

Controlled Experiments on Dark-Matter Halo Structure and Galaxy Morphology I: What Sets Galaxy Sizes?

Guangze Sun,¹ Fangzhou Jiang,^{2*} Jing Wang²

¹Department of Astronomy, Peking University, Beijing 100871, People's Republic of China

²Kavli Institute for Astronomy and Astrophysics, Peking University, Beijing 100871, People's Republic of China

Accepted XXX. Received YYY; in original form ZZZ

ABSTRACT

The properties of galaxies are intricately linked to the characteristics of their host dark-matter haloes. We use a suite of controlled simulations of isolated galaxies to quantify how halo spin, concentration, inner density profile, and baryon fraction regulate galaxy sizes, at fixed halo mass of $M_{\text{vir}} = 10^{11} M_{\odot}$. We generate initial conditions of haloes and inhabitant spherical gas distributions in equilibrium, on a parameter grid spanned by these four halo parameters, and evolve the systems with the GIZMO code and the FIRE-3 physics. The resulting half-mass radii of stars and cold baryons depend systematically on halo structure and baryon content: galaxy size increases with halo spin, decreases with halo concentration, is weakly sensitive to the inner density slope except in highly cuspy haloes, and is strongly suppressed at high baryon fractions. We evaluate the relative importance of the halo parameters on galaxy size using different metrics including the quadratic response-surface method and random-forest regression, and consistently find halo concentration to be the most informative predictor of size. The baryon fraction shows a subtle, non-monotonic impact on size, by modulating how galaxy size depends on halo spin. Our results clarify which secondary parameters of host dark-matter haloes dominate the scatter in galaxy sizes at the massive-dwarf mass scale.

Key words: galaxies: formation – galaxies: haloes – galaxies: dwarf – galaxies: structure

1 INTRODUCTION

In the standard Λ CDM paradigm of structure formation, dark matter (DM) dominates the mass budget and forms gravitationally bound structures, haloes, that provide gravitational potential wells in which galaxies form and evolve (e.g., White & Rees 1978; Blumenthal et al. 1984). Theoretical models and numerical simulations based on this paradigm predict key statistical properties of the halo population, such as their mass function, spatial clustering, and internal structure (e.g., Press & Schechter 1974; Navarro et al. 1996, 1997; Springel et al. 2005). Given these mature theories of DM haloes, a crucial step towards a theoretical framework of galaxy formation lies in establishing the galaxy-halo connection — the set of rules that govern how galaxies populate and evolve within these haloes (see e.g., Wechsler & Tinker 2018, for a review).

A central question in the galaxy–halo connection is how the properties of dark-matter haloes regulate the morphology of their resident galaxies, particularly their characteristic sizes. Halo mass is widely recognized as the primary driver of galaxy morphology, a conclusion supported by several complementary lines of evidence. First, on average, galaxy size exhibits an approximately linear scaling with the virial radius of the host halo (e.g. Kravtsov 2013; Somerville et al. 2018), $R_{\text{gal}} \simeq 0.02 R_{\text{vir}}$. At a given epoch, the virial radius R_{vir} is uniquely determined by halo mass and is commonly inferred from stellar masses using stellar mass–halo mass relations derived from abundance matching (e.g. Moster et al. 2013; Behroozi et al. 2013).

Second, cosmological hydrodynamical simulations show that disc morphologies preferentially arise in haloes above a characteristic mass threshold, $M_{\text{vir}} \gtrsim 10^{11.5} M_{\odot}$ (Dekel et al. 2020; Lapiner et al. 2023; Liang et al. 2025b). At slightly lower masses, $M_{\text{vir}} \sim 10^{11} M_{\odot}$, galaxies display striking morphological diversity, with stellar surface densities spanning more than two orders of magnitude and ultra-diffuse galaxies coexisting alongside compact dwarfs (see e.g. Sales et al. 2022). Thus, while halo mass sets the overall scale of galaxy size and morphology, the substantial scatter around these relations indicates that additional halo properties beyond mass must play an important role in regulating the final extent of galaxies.

The origin of this scatter remains debated. The angular momentum of the dark matter halo, often parameterized by the dimensionless spin parameter λ (Peebles 1969; Bullock et al. 2001), has been considered a primary determinant of galaxy size. Classical models of galaxy formation, assuming conservation of specific angular momentum during baryonic collapse, predict that galaxy size scales with halo spin and virial radius, $R_{\text{gal}} \propto \lambda R_{\text{vir}}$ (e.g., Fall & Efstathiou 1980; Mo et al. 1998).

However, hydrodynamical cosmological simulations reveal surprisingly mixed views and somewhat weak correlation between the spin of a galaxy and that of its host dark-matter halo (Jiang et al. 2019; Rohr et al. 2022). In particular, using two suites of zoom-in simulations, Jiang et al. (2019) find that the galaxy half-stellar-mass radius correlates more tightly with halo concentration and virial radius, following an empirical relation $r_{1/2,\star} \propto c^{-0.7} R_{\text{vir}}$. Focusing on central dwarf galaxies with stellar masses $M_{\star} \sim 10^{7-9} M_{\odot}$ in the FIREbox simulation, Rohr et al. (2022) show that the scatter in

* Corresponding author: fangzhou.jiang@pku.edu.cn

the relation between galaxy half-stellar-mass radius and halo virial radius exhibits little correlation with halo spin (or concentration), suggesting that baryonic processes overwhelm halo properties in setting the sizes of these bright dwarf systems. The strength of these correlations varies across simulation suites. For example, [Liang et al. \(2025a,b\)](#) find that in the IllustrisTNG-50 simulations, galaxy size at fixed halo mass exhibits a modest positive correlation with the halo spin parameter, as well as an anti-correlation with halo concentration. Taken together, these studies indicate that different halo properties and baryonic physics contribute with varying importance, and a unified understanding of the primary drivers of galaxy size at fixed halo mass remains elusive.

In addition to the mixed results from cosmological simulations, many of these studies share a conceptual limitation: the relations between galaxy size and host-halo structure are typically established using instantaneous halo properties, whereas galaxy sizes should, in principle, be more strongly influenced by the properties of their progenitor haloes at the time when the galaxy formed. Using cosmological simulations to connect galaxy properties to progenitor halo structure, however, presents two major challenges. First, there is no consensus on how to define the halo “formation” time. Common definitions include the epoch when a halo first assembles half of its final mass (e.g. [Lacey & Cole 1993](#); [Sheth & Tormen 2004](#)), the end of the fast accretion phase (e.g. [Zhao et al. 2003](#)), or the time of the last major merger (e.g. [Li et al. 2008](#)). It remains unclear which of these definitions most faithfully captures the physically relevant formation epoch for establishing galaxy–halo connections. Second, even if a specific definition is adopted, reconstructing the time evolution of halo structural parameters requires reprocessing particle-level data across all simulation snapshots, which is computationally and storage intensive.

Another limitation of analyses based on cosmological simulations is the restricted range of halo properties that they typically probe. For example, most simulations designed to study dwarf-galaxy structure employ zoom-in techniques or small simulation volumes (e.g. [Wang et al. 2015](#); [Hopkins et al. 2018](#)). While these approaches achieve the numerical resolution required to resolve dwarf morphologies, they inevitably sacrifice statistical power and limit the diversity of halo structural properties. This restriction poses a significant challenge for addressing questions such as how the inner density profile of a host dark-matter halo influences galaxy morphology. In the NIHAO and FIRE-2 simulations, haloes with masses around $10^{11} M_{\odot}$ almost universally develop flat inner density cores ([Freundlich et al. 2020](#); [Lazar et al. 2020](#)), whereas haloes in the IllustrisTNG simulations remain predominantly cuspy across a wide range of halo masses ([Bose et al. 2019](#)).

These considerations motivate complementing cosmological analyses with controlled numerical experiments designed to isolate specific physical dependencies. In controlled simulations, there is no ambiguity in the definition of formation time, as the properties of the system at formation are fully specified by the initial conditions. Moreover, halo parameters can be varied systematically, enabling a wide baseline of halo structural properties by construction.

In this series of studies, we adopt idealized (isolated) galaxy simulations to identify which secondary dark-matter halo properties, beyond halo mass, most strongly regulate galaxy morphology. In this first paper of the series, we focus on a single halo mass, $M_{\text{vir}} = 10^{11} M_{\odot}$, which corresponds to the characteristic halo mass of bright dwarf galaxies and the mass scale at which structural diversity is maximized (e.g. [Di Cintio et al. 2014](#); [Oman et al. 2015](#); [Lazar et al. 2024](#)). We systematically explore how variations in halo spin, concentration, inner density slope, and baryon fraction modu-

late galaxy size at fixed halo mass. In subsequent papers in this series, we plan to extend the analysis to a broader range of halo masses and examine the halo conditions governing additional aspects of galaxy morphology beyond size, such as clumpiness.

This paper is organized as follows. Section 2 describes the design of our parameter grid, the numerical implementation of the hydrodynamical simulations, and the analysis methods. Section 3 presents the correlations between galaxy size and initial halo properties and establishes a rank ordering of the relative importance of these halo parameters in regulating galaxy size. In Section 4, we discuss the implications of our findings for galaxy-size predictors commonly employed in semi-analytic and empirical models. We summarize our conclusions in Section 5. Throughout this work, we define haloes as spherical overdensities of 200 times the critical density of the Universe at $z = 0$, with $\rho_{\text{crit}} = 126.08 M_{\odot} \text{ kpc}^{-3}$, and denote halo virial radius and mass as R_{vir} and M_{vir} , respectively.

2 METHODS

In this section, we present the details of our controlled simulation suite. We describe and motivate the choices of halo parameters and the numerical configurations adopted in our models (Section 2.1), summarize the numerical code GIZMO and the FIRE-3 galaxy-formation prescriptions employed in our simulations (Section 2.2), and outline the analysis tools used in this work (Section 2.3).

2.1 Halo parameters and simulation setups

Here we focus on the impact of halo structural parameters on galaxy size and keep the halo mass fixed at $10^{11} M_{\odot}$. We choose this mass scale for several reasons. First, structural diversity of galaxies is expected to be maximal at this mass (e.g., [Di Cintio et al. 2014](#); [Oman et al. 2015](#); [Lazar et al. 2024](#)). Second, characterizing galaxy sizes is a primary goal of this work, and cosmological simulations show that stable disc galaxies begin to emerge at approximately this halo mass (e.g., [Dekel et al. 2020](#); [Benavides et al. 2025](#)). Third, although more massive haloes ($\sim 10^{12} M_{\odot}$) can also host stable discs, the influence of accreting supermassive black holes is, in principle, non-negligible at those masses, while a proper treatment of such effects is not yet fully captured by current subgrid prescriptions.

That said, we have verified with a set of test simulations spanning different halo masses that our models approximately reproduce key scaling relations, such as the stellar mass–halo mass relation, and exhibit the strongest cusp–core transitions in the halo mass regime characteristic of—and consistent with—those found in cosmological FIRE-2 simulations ([Lazar et al. 2020](#)).

The parameters varied in our simulations are defined as follows.

- **Halo concentration** is defined as $c_2 = R_{\text{vir}}/r_{-2}$, where r_{-2} is the radius at which the logarithmic density slope equals -2 . DM haloes are initialized and fitted using the Dekel-Zhao (DZ) profile ([Freundlich et al. 2020](#)), which introduces one additional degree of freedom relative to the [Navarro et al. \(1997, NFW\)](#) profile and allows direct control of the logarithmic density slope of the halo. The DZ profile is given by:

$$\rho(r) = \frac{\rho_0}{x^a (1 + x^{1/2})^{2(3.5-a)}}, \quad (1)$$

where $x = r/r_c$, with r_c a scale radius defining the concentration $c = R_{\text{vir}}/r_c$. The parameter a specifies the asymptotic inner density slope as $r \rightarrow 0$, and ρ_0 is characteristic density related to the virial

Table 1. Values adopted in the controlled simulations suite for each parameter in the factorial grid of c_2 , s_1 , λ , and f_b , at a fixed halo mass of $M_{\text{vir}} = 10^{11} M_{\odot}$ (see Section 2.1). The bold fonts indicate fiducial values.

Properties	Values
c_2	3, 10 , 20
s_1	0.0, 0.5, 1.0 , 1.5
λ	0.02, 0.04 , 0.06, 0.08
f_b	0.03, 0.07 , 0.14

overdensity Δ via:

$$\rho_0 = (1 - a/3)\bar{\rho}_0, \quad \bar{\rho}_0 = c^3 \mu \Delta \rho_{\text{crit}}, \quad (2)$$

with

$$\mu = c^{a-3} (1 + c^{1/2})^{2(3-a)}. \quad (3)$$

The DZ parameters c and a are not always the most convenient for comparison with the literature. In particular, c differs from the commonly used concentration parameter c_2 , which coincides with the standard NFW definition. The two are related by

$$c_2 \equiv \frac{R_{\text{vir}}}{r_2} = c \left(\frac{1.5}{2-a} \right)^2. \quad (4)$$

- **Inner density slope**, s_1 , is defined as the logarithmic slope $-d \ln \rho / d \ln r$ evaluated at 1% of the virial radius. This quantity can be expressed in terms of the DZ parameters c and a as:

$$s_1 = \frac{a + 3.5c^{1/2}(r_1/R_{\text{vir}})^{1/2}}{1 + c^{1/2}(r_1/R_{\text{vir}})^{1/2}} = \frac{a + 0.35c^{1/2}}{1 + 0.1c^{1/2}}, \quad (5)$$

where $r_1 = 0.01 R_{\text{vir}}$.

- **Halo spin parameter** is defined following (Bullock et al. 2001) as

$$\lambda = \frac{j_{\text{vir}}}{\sqrt{2} R_{\text{vir}} V_{\text{vir}}}, \quad (6)$$

where $j_{\text{vir}} = J_{\text{vir}}/M_{\text{vir}}$ is the specific angular momentum of the halo, and V_{vir} the circular velocity evaluated at the virial radius R_{vir} .

- **The baryon fraction** of a halo, f_b , is defined as the ratio of the total baryonic mass to the virial mass. Here, we emphasize that f_b is not necessarily equal to the cosmic baryon fraction of ≈ 0.165 . Observations of nearby galaxies reveal substantial scatter in baryon fraction across a wide range of halo masses (e.g. Mancera Piña et al. 2025). Consistent with this, cosmological hydrodynamical simulations such as FIRE-2 also show that f_b deviates from the cosmic fraction at halo masses below the Milky Way and exhibits significant scatter (Hafen et al. 2019). We therefore include f_b as a parameter in our grid and explore how variations in f_b affect the resulting galaxy properties. We adopt a fiducial value of 0.07, motivated by the results of Hafen et al.

We construct a nearly factorial parameter grid that samples the four halo properties (c_2 , s_1 , λ , f_b) at the discrete values listed in Table 1. These parameter choices are designed to sample the range of values commonly found in cosmological simulations. For example, halo concentration exhibits a lower bound of ~ 3 , a median value of ~ 10 , and a $\sim 2\sigma$ upper-tail value of ~ 20 at the halo mass of interest (e.g. Dutton & Macciò 2014; Diemer & Kravtsov 2015). Similarly, the halo spin parameter has a median value of ≈ 0.04 , with 0.02 and 0.08 sampling the approximate 2σ tails of the distribution (Bullock et al. 2001). The inner density slope values span the full range relevant to the cusp–core problem (e.g. Bose et al. 2019; Freundlich et al.

2020), from completely flat cores ($s_1 = 0$) to steep cusps ($s_1 = 1.5$). In principle, this grid would yield $3 \times 4 \times 4 \times 3 = 144$ parameter combinations. However, the DZ functional form does not permit physically meaningful solutions for the combination $(c_2, s_1) = (20, 0)$, and we therefore exclude all models with this pairing. The resulting design consists of $N = 132$ distinct simulation runs, which form the main sample analyzed this work.

For each parameter combination, we construct an initial condition (IC) consisting of a DZ DM halo and a gaseous component in approximate hydrostatic equilibrium. There is no unique prescription for establishing exact equilibrium between the gas and the host halo; instead, we follow the approach of Kim & Lee (2013), in which the gas distribution that is initialized to be self-similar to the DM halo and is then allowed to relax toward equilibrium under gravity and hydrodynamics alone.

In practice, we first generate two collisionless haloes with identical structural parameters but particle numbers different by a factor of five, using 10^7 and 2×10^6 particles, respectively, with the MAny-component Galaxy Initializer (MAGI) code. This corresponds to a gas particle mass of $10^4 M_{\odot}$ and a dark-matter particle mass of $5 \times 10^4 M_{\odot}$, with a minimum adaptive gravitational softening of 0.5 pc for gas and constant softening of 30 pc for dark matter, respectively, comparable to the numerical choices by (Hopkins et al. 2018). We then combine these two realizations by randomly designating a fraction f_b of the higher-resolution particles as gas particles and a fraction $(1 - f_b)$ of the lower-resolution particles as DM particles. The resulting composite system is subsequently relaxed in the hydrodynamics solver GIZMO (Hopkins 2015) under gravity and hydrodynamics only.

The initial temperature of the gaseous component is set to the halo virial temperature,

$$T_{\text{vir}} = \frac{\mu m_p}{2k_B} \frac{GM_{\text{vir}}}{R_{\text{vir}}}. \quad (7)$$

We adopt a uniform initial gas metallicity of $Z = 0.003 Z_{\odot}$, following Kim & Lee (2013).

To set the halo spin, we adopt the empirical specific angular-momentum profile proposed by Bullock et al. (2001),

$$j(< M) = g_0 M^{1.3}. \quad (8)$$

Where $j(< M)$ denotes the cumulative specific angular momentum enclosed within mass M . We determine the normalization g_0 by requiring that the integrated angular momentum of the halo reproduces a target spin parameter¹. Given g_0 , we assign the corresponding specific angular momentum to each mass shell and adjust particle velocities accordingly.

We then evolve this configuration for 3 Gyr under gravity and hydrodynamics only, allowing the system to relax. During this relaxation phase, the properties of the gaseous halo evolve slightly. The halo parameters listed in our experimental design (Table 1) therefore correspond to the values measured after this relaxation period. The relaxed systems are subsequently evolved for an additional 3 Gyr using the GIZMO code with full physics enabled. This duration is slightly longer than the dynamical time of a $z = 0$ halo and is sufficient for the galaxies to reach a quasi-steady state. We analyze the galaxy properties at the end of the full-physics simulations and quote the halo properties at the conclusion of the relaxation phase.

¹ This trial target value is different from (slightly higher than) the intended grid value listed in Table 1, because the full-physics simulations are initialized after the system has relaxed, and all quoted values correspond to measurements taken after this relaxation phase.

2.2 Overview of the GIZMO code and the FIRE-3 physics

The simulations are performed using GIZMO (Hopkins 2015), a multi-method gravity plus (magneto)hydrodynamics code, operated in its mesh-free finite-mass (MFM) mode. Gravitational forces are computed using an improved Tree-PM solver from GADGET-3 (Springel 2005).

The simulations incorporate the FIRE-3 physics model (Hopkins et al. 2023), which builds on the FIRE-2 framework with updated stellar evolution models, metal yields, and microphysical prescriptions for gas cooling, heating, and feedback. Gas cooling and heating processes are modeled over a wide temperature range, from 10 to 10^{10} K, including approximate treatments of self-shielding of dense gas from the UV background and from local radiation sources via the LEBRON scheme (Hopkins et al. 2020). Metal-line cooling follows Wiersma et al. (2009) at temperatures $> 10^4$ K, and pre-tabulated CLOUDY rates (Ferland et al. 1998) are used at lower temperatures.

Star formation occurs in gas that is locally self-gravitating (Hopkins et al. 2013), in a converging flow, Jeans unstable, and denser than $n_{\text{th}} = 1000 \text{ cm}^{-3}$. Once these conditions are met, stars form with 100% efficiency per local free-fall time. Each star particle represents a single stellar population, assuming a Kroupa (2001) initial mass function for stars over the mass range $0.1 - 100 M_{\odot}$.

Stellar feedback includes momentum input from radiation pressure in the UV, optical, and infrared, with radiative-transfer effects approximated using the LEBRON scheme, as well as energy, momentum, mass, and metal injection from Type Ia and core-collapse supernovae and stellar mass loss (Fielding et al. 2018). Local photoionization and photoelectric heating from young stars are also modeled.

2.3 Simulation analysis

We developed a custom analysis pipeline for this simulation suite, built primarily on PYNBODY (Pontzen et al. 2013), while incorporating selected routines and conventions from GizmoAnalysis (Wetzel & Garrison-Kimmel 2020) and YT (Turk et al. 2011). For each snapshot, we re-centre the system using the PYNBODY centring routines and rotate the coordinate frame so that the z axis aligns with the direction of the total stellar angular momentum. We then measure halo and galaxy properties. To characterize the host-halo structure, we fit the spherically averaged DM density profile with the DZ profile to obtain the structural parameters c_2 and s_1 using eq. (4) and (5). We use the three-dimensional stellar half-mass radius, $r_{1/2,\star}$, as the main definition for galaxy size.² We also examine the half-mass radius of stars and cold gas with temperature $T < 10^4$ K, $r_{1/2,\star+\text{cg}}$, which we refer to as the size of cold baryon.

To quantitatively characterize the impact of halo parameters on galaxy size, we fit a second-order (quadratic) response-surface model (RSM; Myers et al. 2016) to $y \equiv \log r_{1/2,\star}$ as a function of the four halo parameters. We adopt the predictors $\log c_2$, $\log \lambda$, $\log f_b$, and s_1 , and standardize each predictor u_k using its midpoint $u_{k,0}$ and half-range Δu_k via $z_k = (u_k - u_{k,0})/\Delta u_k$, where $z_k \in [-1, 1]$. The response surface is then modeled as

$$y \approx \beta_0 + \sum_k \beta_{1,k} z_k + \sum_k \beta_{2,k} z_k^2 + \sum_{i < j} \beta_{ij} z_i z_j, \quad (9)$$

² We opt for this morphology-independent metric instead of a disk scale radius because galaxies at this mass scale do not always form stable discs. The simple half-mass radius allows us to robustly characterize the overall spatial extent of the system regardless of whether it is discy, a spheroidal, or irregular.

where β_0 is the intercept, the coefficients $\beta_{1,k}$ represent linear terms, $\beta_{2,k}$ quantify curvature, and β_{ij} capture pairwise interaction terms. With standardized predictors, $\beta_{1,k}$ and $\beta_{2,k}$ describe the local sensitivity and curvature of the response around the fiducial model, respectively, while β_{ij} quantify non-additive couplings between parameters. RSM provides a smooth approximation to the galaxy size across the parameter space and enables an explicit decomposition into main effects (linear plus quadratic terms) and pairwise interactions. Additional details are provided in Appendix A.

3 RESULTS

In this section, we present results from our controlled simulation suite to examine how galaxy size responds to systematic variations in halo structural parameters and baryon fraction at fixed halo mass. We begin with a qualitative overview based on projected density and gas temperature distributions (Section 3.1). We then quantify these trends across the full parameter grid using a quadratic response-surface method to identify the dominant effects (Section 3.2). As a complementary approach, we also employ a random-forest regressor to assess the relative importance of the halo parameters regulating galaxy size (Section 3.3).

3.1 Galaxy size under variation of halo parameters

Figs. 1-4 present the stellar surface density distributions as well as gas temperature maps for a set of simulations where only one halo parameter is varied while the others are fixed at the fiducial values (Table 1). Overlaid on these maps are three reference radii: 2 percent of the virial radius, $0.02R_{\text{vir}}$, the half-stellar-mass radius $r_{1/2,\star}$, and the half-mass radius of stars and cold gas $r_{1/2,\star+\text{cg}}$.

In general, our simulations yield a median $r_{1/2,\star}$ of 1.65 kpc with the 16th and 84th percentiles being 0.63 kpc and 3.66 kpc respectively. Reassuringly, as a reference, the standard scaling relation of $r_{1/2,\star} = 0.02R_{\text{vir}}$ with a scatter of 0.2 dex (Kravtsov 2013; Somerville et al. 2018), corresponds to a median of 1.92 kpc and a range of 1.21 to 3.04 kpc at this halo mass, comparable to the range spanned by our simulated galaxies. Hence, the systematic variations in halo structure explored here can generate the desired diversity of galaxy sizes.³

Increasing the halo spin leads to a clear growth in galaxy size, as shown in Fig. 1. This effect is particularly pronounced for the cold-baryon half-mass radius, $r_{1/2,\star+\text{cg}}$, which increases by nearly a factor of three as the spin parameter increases from 0.02 to 0.08. In contrast, the stellar half-mass radius, $r_{1/2,\star}$, grows more moderately and appears to saturate at $\lambda \gtrsim 0.06$. These trends are qualitatively consistent with the theoretical expectations of Mo et al. (1998); however, they already indicate that galaxy size does not scale linearly with halo spin. We revisit this point in Section 4.

Increasing the halo concentration produces an opposite trend, with higher c_2 yielding systematically smaller discs, as shown in Fig. 2. This effect is generally more pronounced for the cold-baryon half-mass radius, $r_{1/2,\star+\text{cg}}$, than for the stellar half-mass radius, $r_{1/2,\star}$. As the cold disc becomes more compact, the hot gaseous halo reaches deeper into the gravitational potential, as can be seen from the temperature maps in the right columns of Fig. 2.

³ We caution that our simulation suite is a uniform experimental design rather than a cosmological sample, so the percentiles should be interpreted as coverage of the explored parameter space rather than the intrinsic population scatter at fixed halo mass.

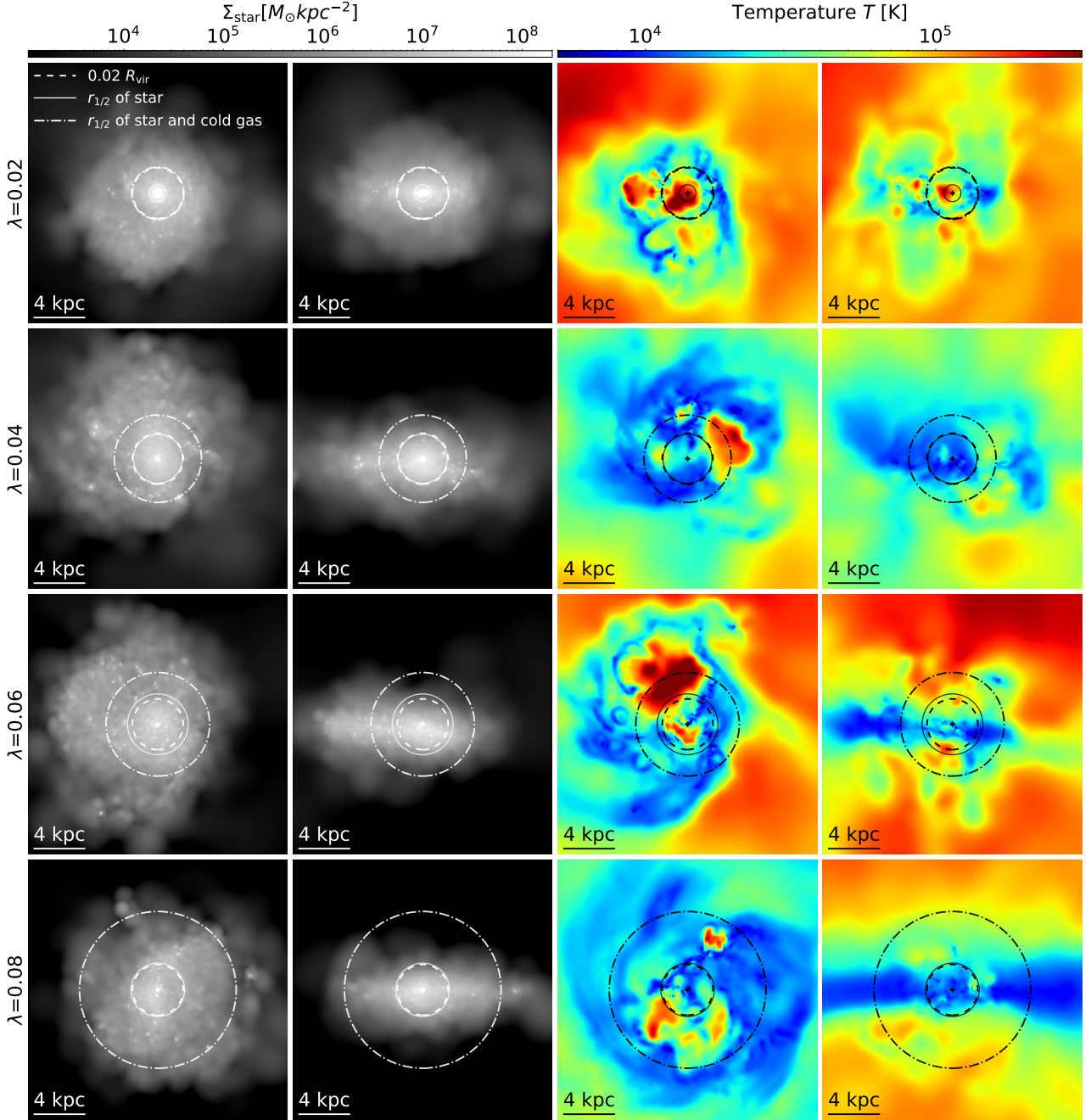


Figure 1. Projected stellar surface density and gas temperature maps for simulations in which the halo spin parameter λ is varied from 0.02 to 0.08 (one value per row, as indicated), while all other parameters are held at their fiducial values: concentration $c_2 = 10$, logarithmic dark-matter-density slope $s_1 = 1$, and baryon fraction $f_b = 0.07$. Columns 1 (2) and 3 (4) show the face-on (edge-on) views. Circles indicate $0.02 R_{\text{vir}}$ (dashed), the stellar half-mass radius $r_{1/2,\star}$ (solid), and the half-mass radius of stars plus cold gas $r_{1/2,\star+\text{cg}}$ (dash-dotted).

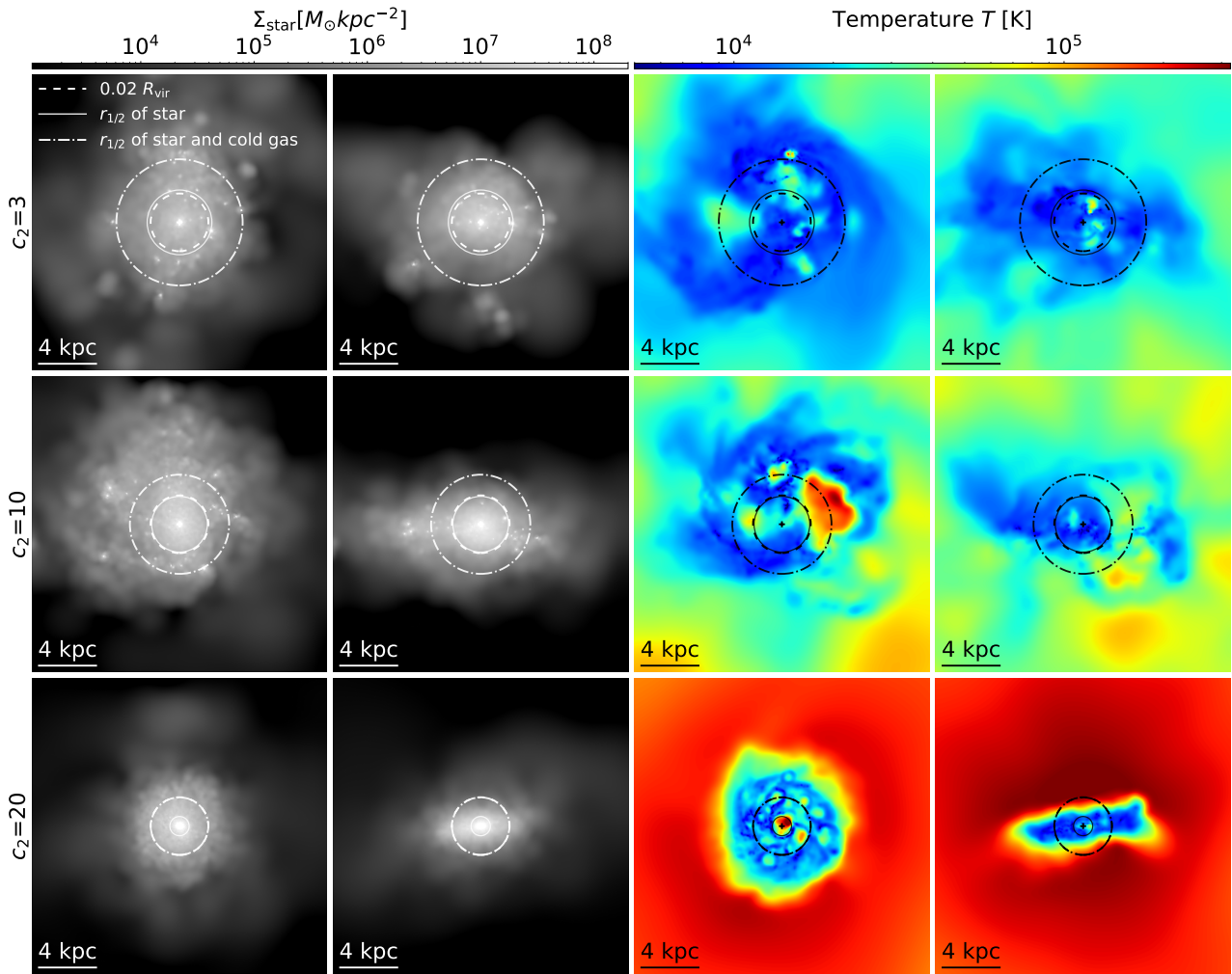


Figure 2. Same as Fig.1, but varying halo concentration c_2 from 3 to 20 while keeping all other parameters at their fiducial values: spin $\lambda = 0.04$, inner DM density slope $s_1 = 1$, and baryon fraction $f_b = 0.07$.

The inner density slope of the DM halo has a more subtle influence on galaxy morphology. While steeper inner slopes tend to enhance the central gas density, the overall galaxy size scales remain similar for $s_1 \lesssim 1$, particularly for the stellar component, whose size remains close to $0.02 R_{\text{vir}}$. For the most cuspy case, $s_1 = 1.5$, however, galaxy sizes, especially the stellar half-mass radius, are significantly reduced.

Varying the baryon fraction f_b has a significant impact on galaxy morphology and size. As shown in Fig. 4, for $f_b \lesssim 0.07$, galaxy sizes are similar, with stellar half-mass radii $r_{1/2,*} \sim 0.02 R_{\text{vir}}$ and cold-baryon half-mass radii $r_{1/2,*+cg}$ approximately twice as large. In this low- f_b regime, the cold gas forms a relatively settled disc, as clearly indicated by the temperature maps. In contrast, at $f_b = 0.14$, which is close to the cosmic baryon fraction, the system undergoes centrally concentrated star formation and develops a compact stellar component. Even the cold gas is no longer arranged in a well-ordered, disc-like configuration. These results imply that the baryon fraction

strongly regulates where gas can reach star-formation conditions, thereby shaping both galaxy morphology and size – an effect that becomes particularly pronounced at high f_b .

We caution that the f_b dependence may be exaggerated in our idealized setup relative to fully cosmological simulations. In our high- f_b model, an amount of gas that is close to the cosmic baryon fraction is initialized instantaneously within the moderately massive halo, rather than being accreted gradually over cosmic time as in a gradually growing halo. As a result, dense central gas may instantly satisfy the star-formation criteria, triggering a central starburst. Despite this caveat, our simplified experiments offer valuable physical insight. First, they suggest that any episode of high baryon fraction in a moderately massive halo (e.g., $M_{\text{vir}} \sim 10^{11} M_{\odot}$) likely leads to the formation of a compact galaxy, even when strong stellar feedback is included through the FIRE-3 physics. Second, baryon fractions below the cosmic mean are a natural requirement for bright dwarf systems to develop extended sizes and discy morphologies.

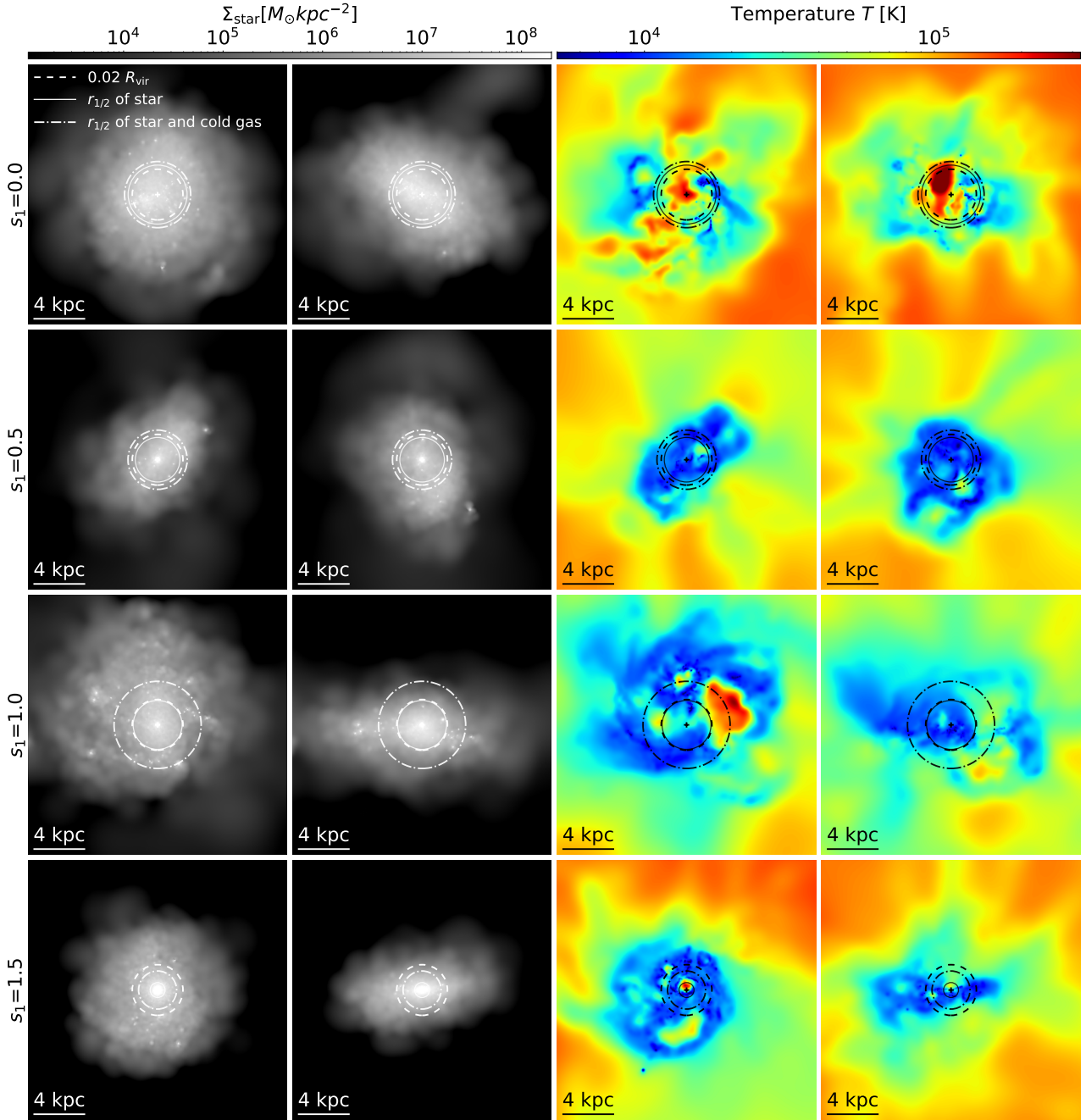


Figure 3. Same as Fig. 1, but varying the inner logarithmic slope of dark matter density s_1 from 0 to 1.5, while keeping all other parameters at their fiducial values: spin $\lambda = 0.04$, concentration $c_2 = 10$, and baryon fraction $f_b = 0.07$.

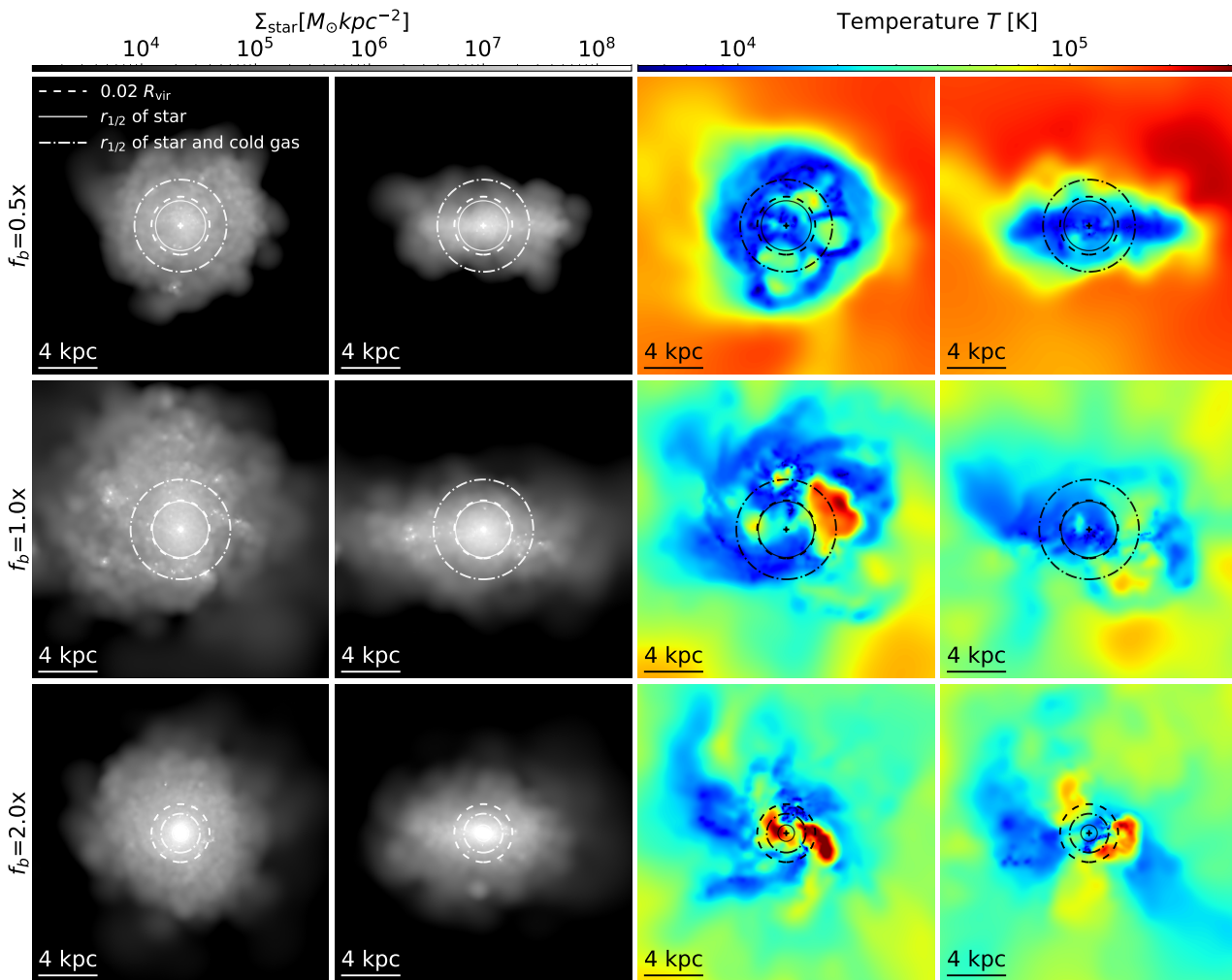


Figure 4. Same as Fig. 1, but varying the baryon fraction f_b relative to the fiducial value of 0.07 (Hafen et al. 2019) from $0.5\times$ to $2.0\times$, while keeping all other parameters at their fiducial values: spin $\lambda = 0.04$, concentration $c_2 = 10$, and logarithmic dark-matter-density slope $s_1 = 1$.

3.2 Quantifying the impact of halo properties on galaxy size

The visual examinations of the density maps and temperature maps in Section 3.1 confirm that all the four parameters impact galaxy morphology and size. It is natural to aim for a quantitative result on the relative importance. Since there is no simple concordance metric for relative importance, we adopt complementary measurements summarized in Table 2.

In this section, we consider two importance proxies. The first is the Pearson correlation coefficient \mathcal{R} between each halo parameter and galaxy size $r_{1/2,*}$. Larger $|\mathcal{R}|$ indicates a tighter linear trend in the marginal sense. The second class of proxies is derived from the fitted quadratic response-surface model (RSM; Section 2.3, eq. 9). For a given factor, we assess its contribution by comparing the full RSM to a reduced model in which selected terms involving that factor are removed and the remaining coefficients are re-estimated. The resulting degradation in fit defines a partial R^2 (coefficient of partial determination), namely the fraction of the residual variance

under the reduced model that is explained by the removed terms. We report both a *main-effect* partial R^2 , obtained by removing the linear and quadratic terms of that factor, and a *total-effect* partial R^2 , which additionally removes all interaction terms involving the same factor (see Appendix A for details).

Fig. 5 shows the correlations between the stellar half-mass radii and individual halo parameters in our simulation suite. Despite substantial scatter at fixed parameter values, the mean trends are clear and broadly consistent with the visual impressions from Figs. 1–4. In particular, $r_{1/2,*}$ increases with halo spin λ , with a Pearson correlation coefficient of $\mathcal{R} = 0.35$, and decreases with both concentration c_2 and inner density slope s_1 , with $\mathcal{R} = -0.49$ and -0.44 , respectively. The overall correlation with f_b appears weak and mildly positive, seemingly at odds with the visual impression from Fig. 4. We caution, however, that this is mainly because the dependence on f_b is often non-monotonic at fixed halo structural parameters. This behavior is evident from the thin lines connecting simulations in the upper

Table 2. Summary of complementary importance proxies used to quantify the dependence of the stellar half-mass radius, $r_{1/2,\star}$, on the four halo parameters. Pearson’s \mathcal{R} measures the marginal linear correlation between each parameter and $r_{1/2,\star}$ across the full simulation sample, with the sign indicating the direction of the trend. The quadratic response-surface model (RSM) provides two conditional effect-size metrics: a main-effect partial R^2 , obtained from a joint (linear + quadratic) coefficient-block test for each parameter, and a total-effect partial R^2 , derived from an analogous block test that additionally includes all pairwise interaction terms involving that parameter (definitions and HC3-robust inference are described in Appendix A). Random-forest (RF) entries report normalized feature importance (each RF row sums to unity across the four parameters); we list four RF estimators—MDI, out-of-fold permutation, OOB permutation, and SHAP (Appendix B).

importance proxy	c_2	λ	s_1	f_b
Pearson \mathcal{R}	-0.49	+0.35	-0.44	+0.20
RSM main-effect partial R^2	0.463	0.477	0.492	0.033
RSM total-effect partial R^2	0.579	0.523	0.544	0.210
RF MDI	0.303	0.241	0.267	0.188
RF permutation (OOF)	0.389	0.231	0.200	0.180
RF permutation (OOB)	0.395	0.235	0.193	0.178
RF SHAP	0.372	0.245	0.255	0.128

right panel of Fig. 5: several runs exhibit a mild increase in galaxy size with f_b at $f_b \lesssim 7$, followed by a decrease at larger f_b , a trend that is particularly pronounced for some cases with $c_2 = 3$ and 10. We have verified that the non-monotonic behavior of the f_b trend is also present at moderate halo spin values ($\lambda \simeq 0.04$ -0.06). Only at the highest spin, galaxy size increases monotonically with f_b , whereas at the lowest spin values galaxy size decreases monotonically with f_b .

This behavior is illustrated more clearly in Fig. 6, which visualizes the best-fit response-surface model in two dimensions by varying pairs of halo parameters at a time. The parameter spaces spanned by the halo structural parameters c_2 , s_1 , and λ exhibit nearly linear gradients, indicating that the effects of individual parameters can, to a good approximation, be treated as additive. A notable exception arises in the parameter spaces involving the baryon fraction f_b , where the contours display pronounced curvature. This behavior can be interpreted in two complementary ways. First, as noted above, at fixed c_2 , s_1 , and λ , the dependence of galaxy size on f_b is generally non-monotonic. Second, the influence of halo concentration and spin on galaxy size becomes significantly stronger at higher baryon fractions ($f_b \gtrsim 0.1$). In this sense, the baryon fraction primarily modulates how sensitively galaxy size responds to halo structure, rather than acting as an independent regulator of size.

3.3 Feature importance ranking from random-forest regression

As a non-parametric complement to the quadratic response-surface model, we train a random-forest regressor (Breiman 2001) to predict the stellar half-mass radius $r_{1/2,\star}$ from the four halo parameters (c_2, s_1, λ, f_b) with sklearn (Pedregosa et al. 2011). Here our goal is not an optimal predictive model, but an importance ranking that is insensitive to the quadratic functional assumption in Section 3.2. After experimenting with multiple importance estimators (Appendix B), the same qualitative hierarchy emerges: halo concentration c_2 is consistently the most informative predictor of galaxy size, with a relative importance score of ~ 0.3 -0.4 depending on the specific metric, while halo spin λ and inner slope s_1 have comparable contributions of ~ 0.2 -0.25, followed by the baryon fraction f_b , which scores ~ 0.15 .

Table 2 summarizes the importance metrics and scores discussed

throughout this section. Halo concentration stands out as the primary size regulator followed by the spin parameter.

4 DISCUSSION

In this section, we compare our simulation results with existing models that predict galaxy size from halo properties and examine how different definitions of galaxy size affect the performance of these size predictors.

4.1 Galaxy size predictors revisited

4.1.1 Comparison with the Mo98 model

The classical disc-formation model of Mo et al. (1998) (Mo98) predicts that galaxy size is primarily determined by the virial radius and spin of the host halo, under the assumption that the baryons forming the galaxy initially share the same specific angular momentum as the halo and retain a fraction of it during galaxy formation. In this framework, the disc half-mass radius is given by

$$r_{1/2,\star} = \frac{1.678}{\sqrt{2}} f_j \lambda R_{\text{vir}} f_c^{-1/2} f_R, \quad (10)$$

where the size scales linearly with the *angular-momentum retention factor*,

$$f_j \equiv j_d/m_d. \quad (11)$$

Here $m_d = M_\star/M_{\text{vir}}$ and $j_d = J_d/J_{\text{vir}}$ denote the mass and angular-momentum fractions of the galaxy relative to its host halo, respectively. The factor f_c characterizes the energy structure of the halo and is defined as the ratio of the halo’s binding energy to that of a singular isothermal sphere of the same mass. The factor f_R accounts for the contraction of the halo in response to the gravitational potential of the disc.

The original Mo98 formula assumes that haloes follow an NFW profile. Here, our simulations adopt the DZ profile in order to allow explicit control over the inner density slope. To enable a fair comparison, we therefore adapt the Mo98 model to DZ haloes and compute a predicted stellar half-mass radius $r_{1/2,\star}^{(\text{Mo98})}$ for each simulation. In practice, this entails computing the factors f_c and f_R factors using the DZ profile, and measuring j_d and m_d directly from the simulated galaxies, strictly following their original definitions based on the stellar mass and stellar angular momentum. Details of our implementation of the Mo98 model for DZ haloes, as well as validation tests, are provided in Appendix C.

The left panel of Fig. 7 compares the Mo98-predicted sizes, $r_{1/2,\star}^{(\text{Mo98})}$, with the stellar half-mass radii measured in the simulations, $r_{1/2,\star}$. The model predictions exhibit a clear systematic offset relative to the simulation results, in that the Mo98 model typically under-predicts galaxy sizes by a factor of ~ 5 . Aside from this systematic offset, however, the model reproduces an approximately linear scaling with the simulated galaxy sizes.

Colour-coding individual galaxies by the angular-momentum retention factor, f_j , reveals that the simulations typically yield values well below unity, spanning a wide range from ~ 0.01 to $\lesssim 1$, with a typical value around $f_j \sim 0.2$. To illustrate this point, we recompute the Mo98 size predictions after artificially boosting the retention factor by a factor of five, as indicated by the open triangles in Fig. 7. This ad hoc correction brings the predicted sizes into close agreement with the one-to-one relation. The failure of the simple angular-momentum retention assumption is expected if star-forming gas is preferentially

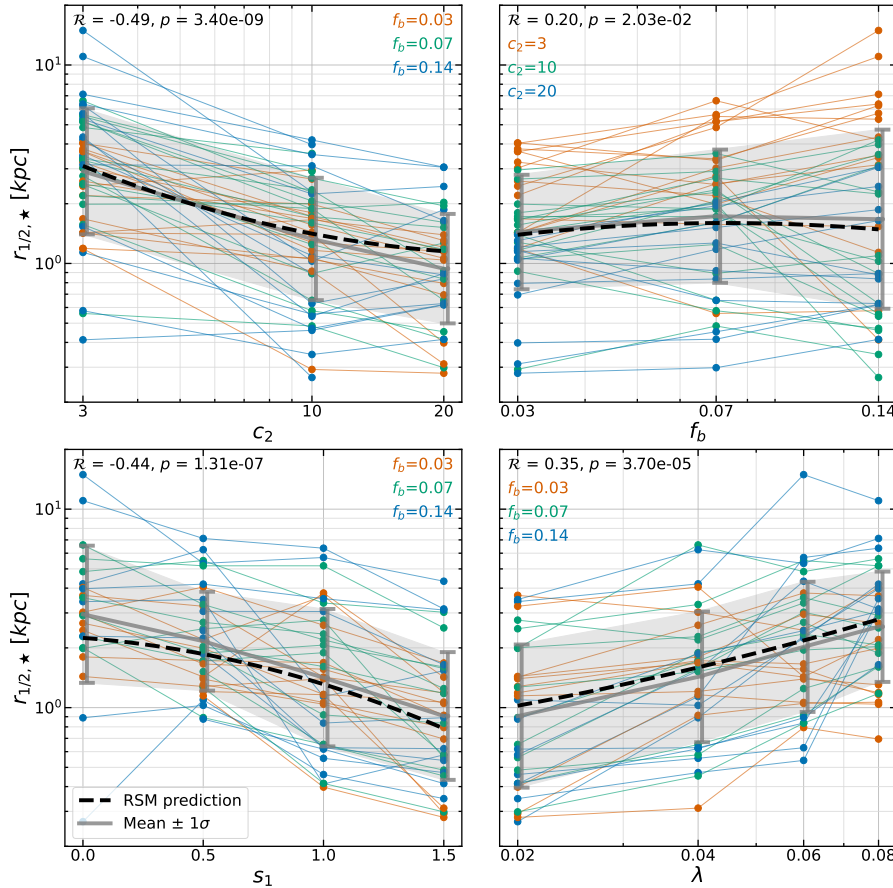


Figure 5. Galaxy size (half-stellar mass radius) as a function of halo structural parameters and baryon fraction. Points represent individual simulation results, coloured by a secondary parameter (f_b or c_2 , as indicated). Thin, colour-matched lines connect simulations in which only the horizontal-axis quantity is varied while all other parameters are fixed. Connected grey symbols show the mean stellar half-mass radius, $r_{1/2,*}$, with error bars and the light-grey bands indicating the 1σ scatter. The symbol positions are slightly offset horizontally to improve visual clarity. The black dashed curve shows the mean prediction of the best-fit quadratic response-surface model (RSM), obtained by varying the parameter of interest while fixing all others at their midpoint values. Pearson correlation coefficients, \mathcal{R} , and the corresponding p -values are quoted.

drawn from the low-angular-momentum tail of the gas distribution and if stellar feedback redistributes angular momentum.

4.1.2 Comparison with simple empirical size predictors

Jiang et al. (2019) (J19) found that galaxy spin (and hence size) is only weakly correlated with halo spin in their cosmological zoom-in simulations. They proposed an empirical, concentration-based size predictor of the form

$$r_{1/2,*} \simeq 0.02(1+z)^{-0.2}(c_2/10)^{-0.7}R_{\text{vir}}. \quad (12)$$

In this relation, the dependence on halo concentration was introduced in part to account for the strong redshift-dependence of the ratio between galaxy size and halo virial radius seen in their cosmological simulations – because the concentration itself evolves with mass and redshift and naturally introduces an implicit redshift dependence. J19 noted that the Mo98 formalism also contains a concentration dependence via the factor f_c . But this dependence is much weaker. Moreover, the redshift dependence of the concentration alone cannot fully explain the redshift dependence of $r_{1/2,*}/R_{\text{vir}}$ seen in the simulations, motivating the introduction of the additional redshift scaling

factor $(1+z)^{-0.2}$. More recently, analyses of large-box cosmological simulations have shown that, even at fixed mass and redshift, disc sizes follow a similar scaling with concentration (Liang et al. 2025a,b). This raises the question of whether the concentration dependence in J19 arises from cosmological assembly effects or instead reflects an imprint of the halo structure itself.

The middle panel of Fig. 7 compares our measured stellar half-mass radii to the J19 predictions.⁴ On average, our idealized isolated simulations reproduce the same qualitative concentration trend reported by J19, suggesting that the dependence of galaxy size on concentration does not require a cosmological environment, but instead emerges from the internal dynamics and galaxy-formation physics within virialized haloes.

The right panel of Fig. 7 compares the measured half-mass radii

⁴ Because the J19 relation depends explicitly on halo concentration and our simulations suite samples three discrete values of concentration, the predicted sizes populate three narrow bands. A small amount of scatter is present because the target values of $c_2 = 3, 10,$ and 20 are those measured after the initial relaxation stage. These values were achieved through trial and error and cannot be matched exactly to the intended targets.

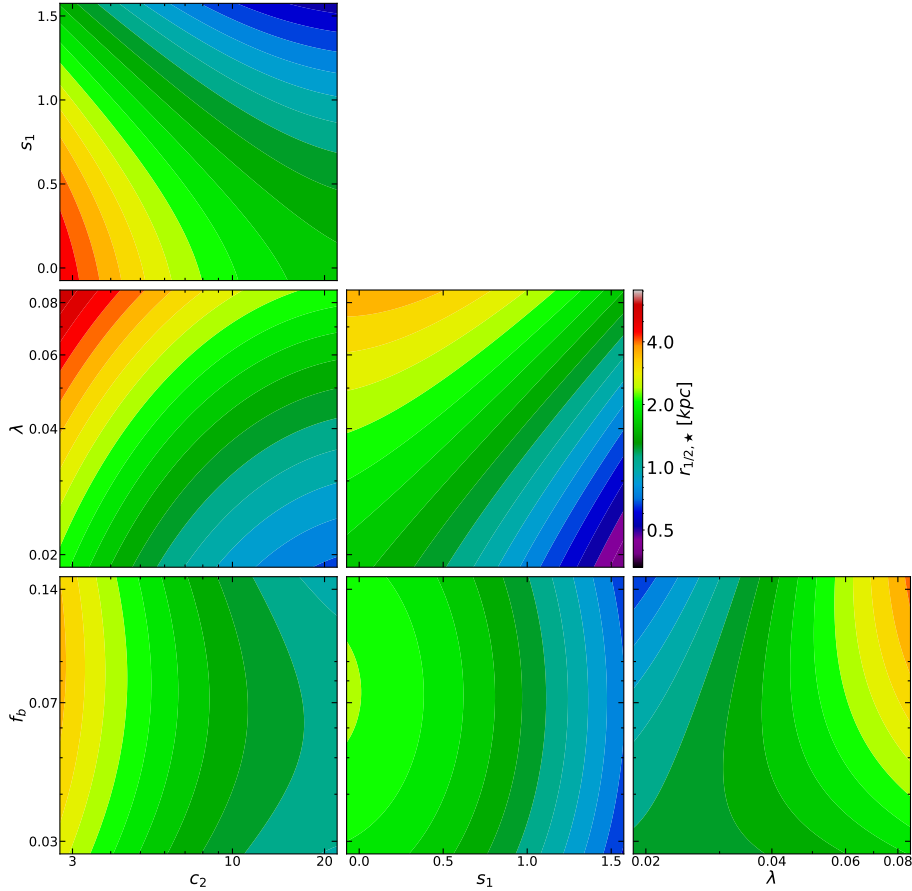


Figure 6. Galaxy size (half-stellar mass radius) as a function of halo structural parameters and baryon fraction, as predicted by the response-surface model fitted to our simulation results. In each panel spanning a pair of parameters, the remaining two parameters are held fixed at their midpoint values. The halo structural parameters exhibit largely additive behavior, reflected by quasi-parallel contours. In contrast, panels involving the baryon fraction show non-separable responses, with the f_b – λ plane displaying the strongest covariance. This indicates that the baryon fraction modulates the sensitivity of galaxy size to variations in halo structure.

to a simple predictor based on halo spin (Somerville et al. 2018),

$$r_{1/2,*} \approx 0.5\lambda R_{\text{vir}}. \quad (13)$$

Both simple empirical models successfully capture the overall trend, but at fixed c_2 or λ , the simulated sizes still span a wide range – colour-coding by the other quantity reveals dependence on the other parameter, consistent with what has been shown in Fig. 6. We therefore conclude that an accurate prescription for galaxy size requires accounting for multiple halo properties rather than relying on any single parameter.

4.2 The impact of the galaxy definition

A practical but often under-emphasized issue in size modeling is that size definitions are not unique. Analytic disc models such as Mo98 are formulated for baryonic discs (stars plus cold gas), whereas many simulation and observational comparisons focus on stellar-only size measurements. Cold or neutral gas discs are usually thinner and more extended than their stellar counterparts: nearby H I surveys find that the ratio of H I to optical size is typically $\gtrsim 1$ –2 (e.g. Broeils & Rhee 1997). Simulations likewise produce neutral-gas discs that extended beyond the stellar body (e.g. Marinacci et al. 2017).

Fig. 8 quantifies the impact of defining the galaxy using stars alone versus stars plus cold gas. The half-mass radius of the cold baryonic component is systematically larger than the stellar-only radius, although the offset is modest compared to the full scatter of the sample. This definition-dependent difference affects the performance of the Mo98 model, in which the predicted disc scale depends explicitly on the angular-momentum retention factor, $f_j = j_d/m_d$.

The inset of Fig. 8 shows that, under a stellar-only definition, most systems lie well below the $j_d = m_d$ relation. When cold gas is included, however, their locations shift toward $j_d = m_d$, indicating more efficient angular-momentum retention. This behavior is consistent with the expectation that a significant fraction of a disc galaxy’s angular momentum resides in the cold gaseous component (e.g. Sales et al. 2010). As a result, the radii predicted by the Mo98 model increase, and the agreement with the measured sizes improves modestly when the galaxy is defined to include both stars and cold gas.

5 CONCLUSIONS

In this paper, we have used a suite of controlled, idealized galaxy simulations to isolate how dark-matter halo structural parame-

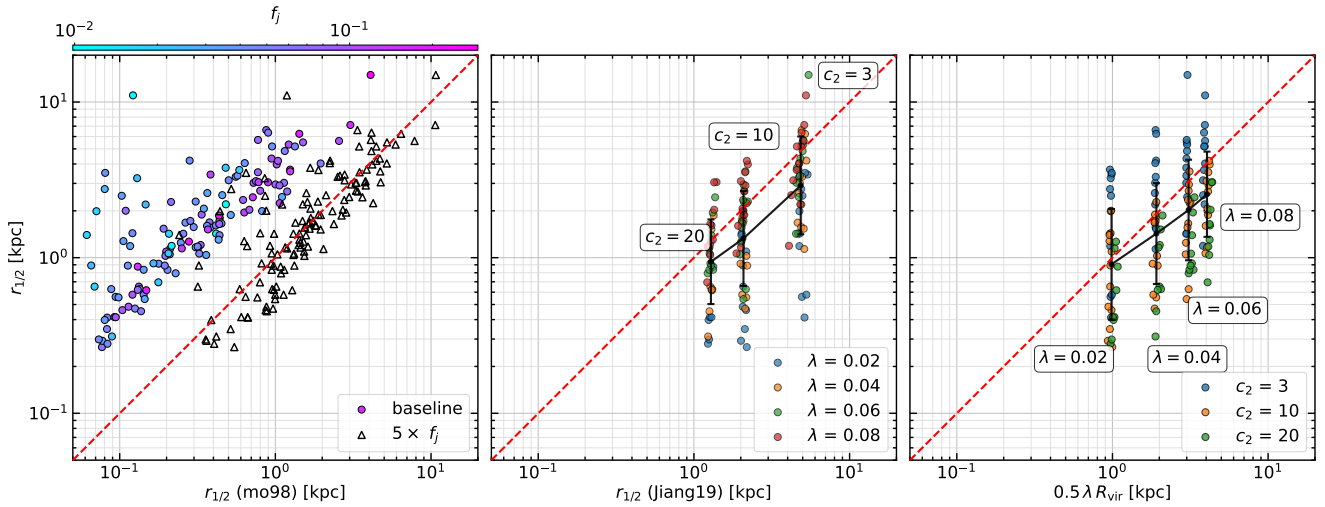


Figure 7. Comparison of simulated galaxy sizes with different size predictors. In all panels, the y-axis shows the measured stellar half-mass radius, $r_{1/2,\star}$, and the red dashed line marks equality. *Left panel:* the [Mo et al. \(1998\)](#) (Mo98) predictor. The x-axis shows the predicted stellar half-mass radius $r_{1/2,\star}^{(\text{Mo98})}$. Filled circles show the predictions and are coloured by the angular-momentum retention factor $f_j \equiv j_d/m_d$. Open triangles illustrate the effect of boosting f_j by a factor of 5, which largely removes the systematic underprediction. *Middle panel:* the [Jiang et al. \(2019\)](#) (J19) concentration-corrected predictor. The x-axis shows the size predicted from the J19 relation $r_{1/2,\star} \approx 0.02(c_2/10)^{-0.7} R_{\text{vir}}$. The three discrete bands of dots correspond to the three c_2 values in our design, as annotated. Symbol colours indicate halo spin λ . *Right panel:* a simple predictor based on the spin parameter: $r_{1/2,\star} \approx 0.5\lambda R_{\text{vir}}$. The discrete four narrow bands of dots correspond to the four λ values used in our simulations, as annotated. Symbol colours indicate halo concentration c_2 . For both *Middle* and *Right* panels, the black points indicate the average $r_{1/2,\star}$ in each bin, with error bars representing the 1σ scatter. While these simple predictors capture the overall trends, they leave substantial scatter at fixed concentration or spin, indicating that additional parameters are required to explain the full diversity.

ters and the initial baryonic mass fraction regulate galaxy size at fixed halo mass, $M_{\text{vir}} = 10^{11} M_{\odot}$. We have run and analyzed 132 GIZMO + FIRE-3 realizations spanning a wide range in halo concentration c_2 , inner density slope s_1 , spin λ , and baryon fraction f_b . For each system, we measured the 3D stellar half-mass radius $r_{1/2,\star}$ and quantified its dependence on halo properties using complementary approaches, including a quadratic response-surface model and a non-parametric random-forest feature-importance ranking.

Across all diagnostics, halo concentration c_2 emerges as the most informative predictor of galaxy size $r_{1/2,\star}$. Halo spin λ provides the next-largest contribution, while the inner-slope s_1 exerts a weaker but still significant influence. The baryon fraction f_b plays a distinct role: rather than acting as a simple, monotonic regulator of size, it primarily modulates how sensitively galaxy size responds to halo structural parameters. In particular, baryon fractions approaching the cosmic mean lead to centrally concentrated star formation and compact galaxies, despite the strong stellar feedback implemented in FIRE-3, whereas lower f_b values favor extended, disc-like systems.

We further revisited widely used analytic and empirical size predictors by comparing their predictions to our controlled simulations. The [Mo et al. \(1998\)](#) model reproduces the overall scaling of galaxy size remarkably well but systematically underpredicts sizes. This is primarily because the simulated galaxies exhibit low angular-momentum retention factors, $f_j \equiv j_d/m_d \ll 1$. This suggests that galaxy formation preferentially draws on low-angular-momentum baryons and that stellar feedback redistributes angular momentum.

The empirical, concentration-based predictor of [Jiang et al. \(2019\)](#) successfully captures the qualitative trend that galaxies in lower-concentration haloes are larger on average, $r_{1/2,\star} \approx 0.02(c_2/10)^{-0.7} R_{\text{vir}}$. Our idealized simulations demonstrate that this dependence does not require a cosmological environment, but instead arises naturally from the internal dynamics and galaxy-formation

physics within virialized haloes. However, the large scatter in $r_{1/2,\star}$ at fixed c_2 underscores the limitations of single-parameter size prescriptions and highlights the need to account for additional halo properties such as spin, inner structure, and baryon content. Similarly, a simple halo-spin-based predictor of $r_{1/2,\star} \approx 0.5\lambda R_{\text{vir}}$ ([Somerville et al. 2018](#)) also successfully captures the overall trend that galaxies in higher-spin haloes are larger, but leaves a large scatter at fixed spin that requires additional modeling.

Finally, we showed that galaxy definition itself matters. Defining the galaxy as stars plus cold gas ($T < 10^4$ K) will systematically increase the half-mass radius relative to a stellar-only definition, consistent with the expectation that cold gas discs are more extended. Including cold gas moves systems closer to $j_d = m_d$, improving angular-momentum retention for the baryonic component and the agreement between Mo98 and the measured sizes.

This work establishes a controlled baseline for understanding how secondary halo properties regulate galaxy sizes at the massive-dwarf scale. Future papers in this series will extend this framework to additional halo masses and to other aspects of galaxy morphology, including substructure driven by feedback, such as clumps, cavities, and asymmetries, and will quantify how these features depend on halo structural conditions.

ACKNOWLEDGEMENTS

We appreciate helpful discussions with Miki Yohei, Hui Li, Florent Renaud, Xi Kang, Suoqing Ji, Houzun Chen, and Jinning Liang. We thank Philip F. Hopkins for sharing the GIZMO simulation code with the FIRE-3 prescriptions. FJ acknowledges support by the National Natural Science Foundation of China (NSFC, Grant No. 12473007) and China Manned Space Program with Grant No. CMS-CSST-2025-A03. We acknowledge the High-performance Computing Platform

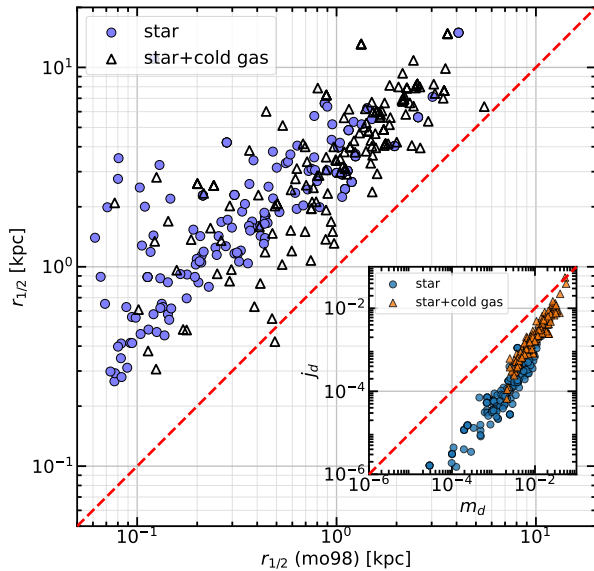


Figure 8. Effect of galaxy definition on the size measurement and on the comparison with the Mo et al. (1998) (Mo98) predictor. The vertical axis shows the galaxy size measured in the simulations, while the horizontal axis shows the size predicted by the Mo98 model. Symbols indicate measurements using either stars only (blue circles) or total cold baryons (stars plus cold gas with $T < 10^4$ K; open triangles). The Mo98 predictions are computed with corresponding definitions of the disc mass fraction, m_d , and the angular-momentum fraction, j_d . The red dashed line marks equality. *Inset:* angular-momentum fraction j_d versus mass fraction m_d for the two galaxy definitions, with the dashed red line indicating $j_d = m_d$. Including cold gas shifts systems closer to $j_d = m_d$, modestly improving the agreement between the Mo98 predictions and the measured sizes.

of Peking University for providing computational resources and support.

DATA AVAILABILITY

The data products and the analysis pipeline are available upon request.

REFERENCES

- Behroozi P. S., Wechsler R. H., Conroy C., 2013, *ApJ*, **770**, 57
 Benavides J. A., et al., 2025, *MNRAS*, **544**, 4651
 Blumenthal G. R., Faber S. M., Primack J. R., Rees M. J., 1984, *Nature*, **311**, 517
 Bose S., et al., 2019, *MNRAS*, **486**, 4790
 Breiman L., 2001, *Machine Learning*, **45**, 5
 Broeils A. H., Rhee M.-H., 1997, *A&A*, **324**, 877
 Bullock J. S., Dekel A., Kolatt T. S., Kravtsov A. V., Klypin A. A., Porciani C., Primack J. R., 2001, *ApJ*, **555**, 240
 Dekel A., Ginzburg O., Jiang F., Freundlich J., Lapiner S., Ceverino D., Primack J., 2020, *MNRAS*, **493**, 4126
 Di Cintio A., Brook C. B., Macciò A. V., Stinson G. S., Knebe A., Dutton A. A., Wadsley J., 2014, *MNRAS*, **437**, 415
 Diemer B., Kravtsov A. V., 2015, *ApJ*, **799**, 108
 Dutton A. A., Macciò A. V., 2014, *MNRAS*, **441**, 3359

- Fall S. M., Efstathiou G., 1980, *MNRAS*, **193**, 189
 Ferland G. J., Korista K. T., Verner D. A., Ferguson J. W., Kingdon J. B., Verner E. M., 1998, *PASP*, **110**, 761
 Fielding D., Quataert E., Martizzi D., 2018, *MNRAS*, **481**, 3325
 Freundlich J., et al., 2020, *MNRAS*, **499**, 2912
 Hafen Z., et al., 2019, *MNRAS*, **488**, 1248
 Hopkins P. F., 2015, *MNRAS*, **450**, 53
 Hopkins P. F., Narayanan D., Murray N., 2013, *MNRAS*, **432**, 2647
 Hopkins P. F., et al., 2018, *MNRAS*, **480**, 800
 Hopkins P. F., Grudić M. Y., Wetzel A., Kereš D., Faucher-Giguère C.-A., Ma X., Murray N., Butcher N., 2020, *MNRAS*, **491**, 3702
 Hopkins P. F., et al., 2023, *MNRAS*, **519**, 3154
 Jiang F., Dekel A., Freundlich J., Romanowsky A. J., Dutton A. A., Macciò A. V., Di Cintio A., 2019, *MNRAS*, **487**, 5272
 Kim J.-h., Lee J., 2013, *MNRAS*, **432**, 1701
 Kravtsov A. V., 2013, *ApJ*, **764**, L31
 Kroupa P., 2001, *MNRAS*, **322**, 231
 Lacey C., Cole S., 1993, *MNRAS*, **262**, 627
 Lapiner S., et al., 2023, *MNRAS*, **522**, 4515
 Lazar A., et al., 2020, *MNRAS*, **497**, 2393
 Lazar I., Kaviraj S., Watkins A. E., Martin G., Bichang'a B., Jackson R. A., 2024, *MNRAS*, **529**, 499
 Li Y., Mo H. J., Gao L., 2008, *MNRAS*, **389**, 1419
 Liang J., Jiang F., Mo H., Benson A., Hopkins P. F., Dekel A., Ho L. C., 2025a, *arXiv e-prints*, p. arXiv:2512.13822
 Liang J., Jiang F., Mo H., Benson A., Dekel A., Tavron N., Hopkins P. F., Ho L. C., 2025b, *MNRAS*, **541**, 2304
 Lundberg S., Lee S.-I., 2017, *arXiv e-prints*, p. arXiv:1705.07874
 Mancera Piña P. E., Read J. I., Kim S., Marasco A., Benavides J. A., Glowacki M., Pezzulli G., Lagos C. d. P., 2025, *A&A*, **699**, A311
 Marinacci F., Grand R. J. J., Pakmor R., Springel V., Gómez F. A., Frenk C. S., White S. D. M., 2017, *MNRAS*, **466**, 3859
 Mo H. J., Mao S., White S. D. M., 1998, *MNRAS*, **295**, 319
 Moster B. P., Naab T., White S. D. M., 2013, *MNRAS*, **428**, 3121
 Myers R. H., Montgomery D. C., Anderson-Cook C. M., 2016, *Response Surface Methodology: Process and Product Optimization Using Designed Experiments*, 4 edn. Wiley Series in Probability and Statistics, John Wiley & Sons, <https://books.google.com/books?id=YFSzCgAAQBAJ>
 Navarro J. F., Frenk C. S., White S. D. M., 1996, *ApJ*, **462**, 563
 Navarro J. F., Frenk C. S., White S. D. M., 1997, *ApJ*, **490**, 493
 Oman K. A., et al., 2015, *MNRAS*, **452**, 3650
 Pedregosa F., et al., 2011, *Journal of Machine Learning Research*, **12**, 2825
 Peebles P. J. E., 1969, *ApJ*, **155**, 393
 Pontzen A., Roškar R., Stinson G., Woods R., 2013, pynbody: N-Body/SPH analysis for python, Astrophysics Source Code Library, record ascl:1305.002 (ascl:1305.002)
 Press W. H., Schechter P., 1974, *ApJ*, **187**, 425
 Rohr E., et al., 2022, *MNRAS*, **510**, 3967
 Sales L. V., Navarro J. F., Schaye J., Dalla Vecchia C., Springel V., Booth C. M., 2010, *MNRAS*, **409**, 1541
 Sales L. V., Wetzel A., Fattahi A., 2022, *Nature Astronomy*, **6**, 897
 Sheth R. K., Tormen G., 2004, *MNRAS*, **349**, 1464
 Somerville R. S., et al., 2018, *MNRAS*, **473**, 2714
 Springel V., 2005, *MNRAS*, **364**, 1105
 Springel V., et al., 2005, *Nature*, **435**, 629
 Turk M. J., Smith B. D., Oishi J. S., Skory S., Skillman S. W., Abel T., Norman M. L., 2011, *ApJS*, **192**, 9
 Wang L., Dutton A. A., Stinson G. S., Macciò A. V., Penzo C., Kang X., Keller B. W., Wadsley J., 2015, *MNRAS*, **454**, 83
 Wechsler R. H., Tinker J. L., 2018, *ARA&A*, **56**, 435
 Wetzel A., Garrison-Kimmel S., 2020, *GizmoAnalysis: Read and analyze Gizmo simulations*, Astrophysics Source Code Library, record ascl:2002.015
 White S. D. M., Rees M. J., 1978, *MNRAS*, **183**, 341
 Wiersma R. P. C., Schaye J., Theuns T., Dalla Vecchia C., Tornatore L., 2009, *MNRAS*, **399**, 574
 Zhao D. H., Mo H. J., Jing Y. P., Börner G., 2003, *MNRAS*, **339**, 12

APPENDIX A: QUADRATIC RESPONSE-SURFACE ANALYSIS

A1 Fitting overview

In this Appendix we summarize the technical details of the quadratic response-surface model used in Section 3.2. For each simulation in the $M_{\text{vir}} = 10^{11} M_{\odot}$ grid we consider four halo predictors: concentration c_2 , spin parameter λ , baryon fraction f_b , and inner-slope proxy s_1 . We work with transformed variables that reflect their natural scaling: $\log c_2$, $\log \lambda$, and $\log f_b$ are used, while s_1 is kept on its original (linear) scale. For each transformed predictor u_k we choose a reference value $u_{k,0}$ (the midpoint of the sampled range) and a half-range Δu_k , and define a dimensionless standardized coordinate

$$z_k \equiv \frac{u_k - u_{k,0}}{\Delta u_k}, \quad (\text{A1})$$

so that $z_k \approx -1$ and $+1$ correspond to the low and high settings in the design, and $z_k = 0$ corresponds to the fiducial model. The response variable is the natural logarithm of the 3D stellar half-mass radius, $y \equiv \log r_{1/2,\star}$, so multiplicative changes in size become additive shifts in y . In terms of the standardized predictors the quadratic response-surface model can be written as

$$y = \beta_0 + \sum_k \beta_{1,k} z_k + \sum_k \beta_{2,k} z_k^2 + \sum_{i < j} \beta_{ij} z_i z_j + \varepsilon, \quad (\text{A2})$$

where β_0 is the intercept, $\beta_{1,k}$ are the local linear slopes, $\beta_{2,k}$ describe curvature in each direction, β_{ij} encode pairwise interactions, and ε denotes the residuals. With four predictors this model contains 15 coefficients including the intercept. The chosen coding has the useful property that β_0 represents the mean $\log r_{1/2,\star}$ at the midpoints of the design, while the $\beta_{1,k}$ quantify the first-order sensitivity of galaxy size to each halo parameter around this reference point.

We estimate the coefficients by ordinary least squares (OLS), treating the simulation grid as a fixed experimental design. However, we do not rely on the usual OLS formula for uncertainties. Standard residual tests applied to an initial (non-robust) fit reveal significant departures from homoskedasticity: both the Breusch–Pagan and White tests reject the hypothesis of constant residual variance. In this regime we adopt the HC3 heteroskedasticity-consistent covariance estimator as implemented in `statsmodels`. HC3 down-weights high-leverage points more strongly than simpler corrections (HC0/HC1) and yields more conservative small-sample inference. Throughout the paper we therefore quote OLS point estimates for the coefficients, but base all t - and F -tests, confidence intervals, and derived uncertainties on the HC3 covariance matrix. The design is well-conditioned: variance-inflation factors for all regression terms are close to unity ($\text{VIF} \lesssim 1.3$), indicating that collinearity among the standardized predictors is not a concern.

For the full $N = 132$ sample at $M_{\text{vir}} = 10^{11} M_{\odot}$, the quadratic response surface provides a good global description of the size response. The coefficient of determination is $R^2 \approx 0.80$ (adjusted $R^2 \approx 0.78$), with an overall F -statistic $F_{14,117} \approx 36.4$ and $p \approx 5 \times 10^{-36}$. The root-mean-square residual in $\log r_{1/2,\star}$ is ≈ 0.37 , corresponding to a 1σ scatter of ≈ 0.16 dex, or a multiplicative factor of ~ 1.5 in physical radius. Only a handful of runs have large studentized residuals or are flagged as influential by Cook’s-distance and leverage thresholds. Re-fitting the model after removing these high-influence cases increases R^2 to ≈ 0.86 and leaves the main-effect curves unchanged within uncertainties, indicating that our conclusions are not sensitive to a small subset of outlying realisations.

A2 Importance proxies from coefficient-block tests

Table 2 reports two importance proxies derived from the response-surface model. Both are based on joint Wald tests on blocks of coefficients using the HC3 covariance matrix. For a block test with statistic F , numerator degrees of freedom d , and residual degrees of freedom ν , we convert the result into an effect-size proxy on a 0–1 scale via

$$R_{\text{partial}}^2 \equiv \frac{dF}{dF + \nu}. \quad (\text{A3})$$

This quantity is closely related to the “partial η^2 ” used in analysis-of-variance settings; in our context it provides a convenient, approximate measure of the additional (conditional) variance explained by the tested block given the rest of the model. Because it is conditional on the other terms in the regression, it is not additive across factors and should be interpreted comparatively.

For the main-effect proxy we test the joint contribution of the linear and quadratic terms of each factor, $(\beta_{1,k}, \beta_{2,k})$ ($d = 2$). This yields large and highly significant partial R^2 values for c_2 , λ , and s_1 (all ≈ 0.46 – 0.49 with $p_F \ll 10^{-6}$), and a much smaller, non-significant value for f_b (partial $R^2 \approx 0.03$ with $p_F \approx 0.14$). For the total-effect proxy we expand the tested block to include the linear and quadratic terms *plus* all interactions involving the factor (five coefficients in total; $d = 5$). In this case, c_2 , λ , and s_1 remain in a high-importance tier (partial $R^2 \approx 0.52$ – 0.58), while the importance of f_b increases substantially (partial $R^2 \approx 0.21$) owing to its coupling with spin. This is consistent with Fig. 6, where the (f_b, λ) panel shows the clearest non-separable behavior.

APPENDIX B: RANDOM-FOREST TRAINING AND FEATURE-IMPORTANCE DEFINITIONS

B1 Model setup and global hyper-parameter tuning

We model the mapping from halo parameters to galaxy size using a random-forest regressor (RF; Breiman 2001). Each RF consists of an ensemble of decision trees trained on bootstrap resamples of the training set, and predictions are obtained by averaging over trees. Because tree-based models are invariant to monotonic feature rescalings and do not require feature standardization, we train directly on the physical input parameters (c_2, s_1, λ, f_b) .

We select the RF hyper-parameters with a single global `GridSearchCV` pass on the full $N = 132$ sample, using 5-fold CV and the negative mean-squared error as the scoring function. The explored grid is

$$\begin{aligned} n_{\text{est}} &\in \{300, 600, 800, 1000, 1200, 1500\}, \\ \text{max_depth} &\in \{\text{None}, 5, 10, 15\}, \\ \text{min_samples_leaf} &\in \{1, 2, 3, 5\}, \\ \text{max_features} &\in \{\text{sqrt}, 1.0\}. \end{aligned}$$

The best-performing configuration is

$$\begin{aligned} n_{\text{est}} &= 1000, \\ \text{max_depth} &= 10, \\ \text{min_samples_leaf} &= 1, \\ \text{max_features} &= \text{sqrt}. \end{aligned}$$

with bootstrap sampling enabled and `oob_score=True`. These hyper-parameters are then held fixed for all subsequent resampling experiments to avoid confounding the stability of feature importances with repeated re-tuning.

B2 Repeated cross-validation protocol and model diagnostics

To assess the robustness of importance rankings to the limited sample size and to the particular train/validation partition, we perform repeated K -fold cross-validation with $K = 5$ and $N_{\text{rep}} = 20$, yielding 100 train/validation splits. Each split trains on $\approx 4/5$ of the sample (~ 105 – 106 runs) and evaluates on the held-out fold (~ 26 – 27 runs). We report standard performance diagnostics to ensure that the RF captures genuine signal: over the 100 splits, the out-of-fold coefficient of determination is $\langle R_{\text{valid}}^2 \rangle \approx 0.64$ with scatter $\sigma(R_{\text{valid}}^2) \approx 0.19$. The out-of-bag score, computed internally on OOB samples within each training fold, is comparably high and substantially more stable, $\langle R_{\text{OOB}}^2 \rangle \approx 0.64$ with $\sigma(R_{\text{OOB}}^2) \approx 0.05$. This indicates that the trained forests are not dominated by pathological overfitting in individual splits, and that importance estimates can be meaningfully aggregated across repeats.

B3 Feature-importance estimators

We quantify feature importance using four complementary estimators that probe different notions of ‘‘importance’’:

- (i) **Mean decrease in impurity (MDI).** We use the standard impurity-based importance returned by the RF implementation, which measures the average reduction in within-node variance attributable to each feature, accumulated over all splits and trees.
- (ii) **Out-of-fold (OOF) permutation importance.** For each CV split, we evaluate the baseline validation-set mean-squared error $\text{MSE}_{\text{valid}}$, then randomly permute a single feature column x_j in the validation set (holding all other columns fixed) and re-evaluate $\text{MSE}_{\text{valid}}^{\pi_j}$. The permutation importance is the performance degradation

$$I_j^{\text{perm}} \equiv \text{MSE}_{\text{valid}}^{\pi_j} - \text{MSE}_{\text{valid}}, \quad (\text{B1})$$
 averaged over repeated shuffles. This estimator directly measures how much predictive accuracy is lost when the information in x_j is destroyed out of sample.
- (iii) **Out-of-bag (OOB) permutation importance.** For each tree in the forest, we identify its OOB subset (samples not included in the bootstrap draw for that tree). We compute a baseline OOB error for that tree, then permute feature x_j within the OOB subset and recompute the error. The per-tree degradation is averaged over trees (and repeated permutations) to obtain an OOB-based permutation importance. Compared to OOF permutation, this avoids using the held-out validation fold and instead exploits the bootstrap structure of the RF.
- (iv) **SHAP-based global importance.** We compute Shapley-style additive explanations (SHAP) for tree ensembles using a Tree-Explainer approach (e.g. Lundberg & Lee 2017). For each split we summarise global importance by the mean absolute SHAP value of each feature over the validation fold, $\langle |\text{SHAP}_j| \rangle$, which measures the typical magnitude of the feature’s contribution to the model output.

Because these estimators live on different scales (and permutation scores can occasionally be slightly negative in finite samples), we convert each split-level importance vector into a normalised score that is comparable within a method:

$$\tilde{I}_j \equiv \frac{\max(I_j, 0)}{\sum_k \max(I_k, 0)}, \quad (\text{B2})$$

so that $\sum_k \tilde{I}_k = 1$ for each estimator and split.

B4 Aggregation, composite score, and resulting hierarchy

Table 2 reports, for each RF estimator, the mean of \tilde{I}_j over the 100 repeated-CV splits. We also define a **composite** RF importance as the arithmetic mean of the four normalised estimators (MDI, OOF permutation, OOB permutation, and SHAP) for each split, followed by averaging over splits. The composite scores show a stable ordering

$$c_2 > (\lambda \approx s_1) > f_b,$$

with c_2 consistently dominant and f_b consistently least important. The robustness is also evident in rank stability: c_2 is ranked first in the overwhelming majority of resamples (depending on estimator, ~ 80 – 100% of splits), while f_b is almost always ranked last. The relative ordering between λ and s_1 varies mildly with the estimator (permutation-based metrics tend to favour λ , whereas MDI/SHAP slightly favour s_1), motivating our conservative conclusion that they occupy a shared intermediate tier.

APPENDIX C: TRANSPLANTING THE MO98 FORMALISM TO THE DEKEL–ZHAO HALO PROFILE

C1 A root-finding solver for the Mo98 disc scale length

The classical disc-formation model of Mo et al. (1998, hereafter Mo98) assumes that a fraction m_d of the halo virial mass M_{vir} settles into a rotationally supported exponential disc and retains a fraction j_d of the halo angular momentum.⁵ The disc surface density is

$$\Sigma(R) = \frac{M_d}{2\pi R_d^2} \exp\left(-\frac{R}{R_d}\right), \quad M_d = m_d M_{\text{vir}}, \quad (\text{C1})$$

and the disc angular momentum for a given circular-velocity curve $V_c(R)$ is

$$\begin{aligned} J_d(R_d) &= 2\pi \int_0^\infty \Sigma(R) V_c(R; R_d) R^2 dR \\ &= M_d R_d \int_0^\infty e^{-u} u^2 V_c(u R_d; R_d) du, \end{aligned} \quad (\text{C2})$$

where $u \equiv R/R_d$. The target angular momentum is $J_d = j_d J_h$, with the halo angular momentum J_h obtained from the Peebles spin parameter (Mo98 eq. 9),

$$\lambda \equiv \frac{J_h |E_h|^{1/2}}{G M_{\text{vir}}^{5/2}} \implies J_h = \lambda \frac{G M_{\text{vir}}^{5/2}}{|E_h|^{1/2}}. \quad (\text{C3})$$

Writing the halo total energy in the standard form

$$E_h = -\frac{1}{2} f_h M_{\text{vir}} V_{\text{vir}}^2 = -\frac{G M_{\text{vir}}^2}{2 R_{\text{vir}}} f_h, \quad V_{\text{vir}}^2 \equiv \frac{G M_{\text{vir}}}{R_{\text{vir}}}, \quad (\text{C4})$$

one can rewrite eq. (C3) as

$$J_h = \lambda M_{\text{vir}} R_{\text{vir}} V_{\text{vir}} \sqrt{\frac{2}{f_h}}. \quad (\text{C5})$$

For an NFW halo, Mo98 give $E_h = -(G M_{\text{vir}}^2 / 2 R_{\text{vir}}) f_c$ (Mo98 eq. 22), with

$$f_c(c) = \frac{c}{2} \frac{1 - (1+c)^{-2} - 2 \ln(1+c)/(1+c)}{[c/(1+c) - \ln(1+c)]^2} \quad (\text{C6})$$

(Mo98 eq. 23), where c is the concentration.

⁵ In the main text we often use the retention factor $f_j \equiv j_d/m_d$.

In Mo98 the disc scale length is obtained by rewriting the condition $J_d = j_d J_h$ into a fixed-point form (their eqs. 28–29) and iterating. However, the iterative scheme is not essential: for any specified initial halo profile (NFW in Mo98; DZ in our work), the adiabatic-contraction calculation always starts from the same unperturbed halo, so the mapping $R_d \mapsto J_d(R_d)$ is deterministic. One may therefore solve for R_d directly as a one-dimensional root-finding problem,

$$\mathcal{F}(R_d) \equiv J_d(R_d) - j_d J_h = 0, \quad (\text{C7})$$

where $J_d(R_d)$ is evaluated by direct numerical integration of eq. (C2).

Evaluating $V_c(R; R_d)$ follows Mo98: the halo responds adiabatically to the slow assembly of the disc, conserving $rM(r)$ for each shell,

$$r_i M_i(r_i) = r M_f(r), \quad (\text{C8})$$

where $M_i(r)$ is the initial halo enclosed mass profile, and

$$M_f(r) = M_d(r) + M_h(r), \quad M_h(r) = (1 - m_d) M_i(r_i). \quad (\text{C9})$$

The cumulative mass of an exponential disc is (Mo98 eq. 26)

$$M_d(r) = M_d \left[1 - \left(1 + \frac{r}{R_d} \right) e^{-r/R_d} \right]. \quad (\text{C10})$$

The total rotation curve is then

$$V_c^2(r) = V_d^2(r) + V_h^2(r), \quad V_h^2(r) = \frac{GM_h(r)}{r}, \quad (\text{C11})$$

with the thin exponential-disc contribution

$$V_d^2(r) = \frac{GM_d}{2R_d} y^2 \left[I_0(y)K_0(y) - I_1(y)K_1(y) \right], \quad y \equiv \frac{r}{2R_d}, \quad (\text{C12})$$

where I_n and K_n are modified Bessel functions. In practice, eq. (C7) can be solved robustly with a bracketing method (e.g. Brent’s algorithm), and is typically fast on modern hardware while being conceptually more transparent than an explicit fixed-point iteration.

C2 Dekel-Zhao haloes: $M(r)$ and f_{DZ}

To transplant the Mo98 machinery to a Dekel–Zhao (DZ) halo (Freundlich et al. 2020), only two halo-specific ingredients are required: (i) the initial enclosed mass profile $M_i(r)$ entering the adiabatic-contraction step (eq. C8); and (ii) the energy factor f_h entering the spin–angular-momentum conversion (eq. C5).

The DZ density profile is (Freundlich et al. 2020, eq. 11)

$$\rho(r) = \frac{\rho_c}{x^a (1 + x^{1/2})^{2(3.5-a)}}, \quad x \equiv \frac{r}{r_c}, \quad c \equiv \frac{R_{\text{vir}}}{r_c}, \quad (\text{C13})$$

with inner-slope parameter a and concentration c . It is convenient to define the compact variable

$$\chi(x) \equiv \frac{x^{1/2}}{1 + x^{1/2}}, \quad \chi_c \equiv \chi(c) = \frac{c^{1/2}}{1 + c^{1/2}}. \quad (\text{C14})$$

Then the enclosed mass takes the simple closed form

$$M_i(r) = M_{\text{vir}} \left(\frac{\chi}{\chi_c} \right)^{6-2a}. \quad (\text{C15})$$

For the total energy, we define the DZ analogue of the NFW energy factor by

$$E_h \equiv -\frac{GM_{\text{vir}}^2}{2R_{\text{vir}}} f_{\text{DZ}}(a, c) = -\frac{1}{2} f_{\text{DZ}}(a, c) M_{\text{vir}} V_{\text{vir}}^2. \quad (\text{C16})$$

Assuming circular orbits for the virialised halo and using the virial theorem, one obtains

$$f_{\text{DZ}}(a, c) = \frac{2(3-a)c}{\chi_c^{12-4a}} B(\chi_c; 10-4a, 3), \quad (\text{C17})$$

where $B(z; p, q)$ is the (unnormalised) incomplete beta function,

$$B(z; p, q) \equiv \int_0^z t^{p-1} (1-t)^{q-1} dt, \quad (\text{C18})$$

and the integral converges for the parameter range relevant here (in particular $a < 2.5$ so that $p = 10 - 4a > 0$).

With eqs. (C15) and (C17), the Mo98 procedure carries over verbatim: in the contraction step, replace the NFW $M_i(r)$ by the DZ mass profile; in the spin conversion, replace $f_c(c)$ by $f_{\text{DZ}}(a, c)$. The disc scale length R_d is then obtained by solving the same root condition, eq. (C7).

This paper has been typeset from a \LaTeX file prepared by the author.